TOPICAL REVIEW

Vanadium oxide, vanadium oxynitride, and cobalt oxynitride as electrocatalysts for the nitrogen reduction reaction: a review of recent developments

IOP Publishing Journal of Physics: Condensed Matter
J. Phys.: Condens. Matter **35** (2023) 333002 (13pp) https://doi.org/10.1088/1361-648X/acd49d

Topical Review

Vanadium oxide, vanadium oxynitride, and cobalt oxynitride as electrocatalysts for the nitrogen reduction reaction: a review of recent developments

Kabirat Balogun[1], Ashwin Ganesan[1], Precious Chukwunenye[1], Mojgan Gharaee[1], Qasim Adesope[1], Slavomir Nemšák[2], Paul S Bagus[1], Thomas R Cundari[1], Francis D'Souza[1] and Jeffry A Kelber[1,*]

[1] Department of Chemistry, University of North Texas, Denton, TX 76203, United States of America
[2] Advanced Light Source, Lawrence Berkeley National Laboratory, Berkeley, CA 94720, United States of America

E-mail: Jeffry.kelber@unt.edu

Received 3 February 2023, revised 4 April 2023
Accepted for publication 11 May 2023
Published 22 May 2023

Abstract

The electrocatalytic reduction of molecular nitrogen to ammonia—the nitrogen reduction reaction (NRR)—is of broad interest as an environmentally- and energy-friendly alternative to the Haber–Bosch process for agricultural and emerging energy applications. Herein, we review our recent findings from collaborative electrochemistry/surface science/theoretical studies that counter several commonly held assumptions regarding transition metal oxynitrides and oxides as NRR catalysts. Specifically, we find that for the vanadium oxide, vanadium oxynitride, and cobalt oxynitride systems, (a) there is no Mars–van Krevelen mechanism and that the reduction of lattice nitrogen and N_2 to NH_3 occurs by parallel reaction mechanisms at O-ligated metal sites without incorporation of N into the oxide lattice; and (b) that NRR and the hydrogen evolution reaction do occur in concert under the conditions studied for Co oxynitride, but not for V oxynitride. Additionally, these results highlight the importance of both O-ligation of the V or Co center for metal-binding of dinitrogen, and the importance of N in stabilizing the transition metal cation in an intermediate oxidation state, for effective N≡N bond activation. This review also highlights the importance and limitations of *ex situ* and *in situ* photoemission—involving controlled transfer between ultra-high vacuum and electrochemistry environments, and of *operando* near ambient pressure photoemission coupled with *in situ* studies, in elucidating the complex chemistry relevant to the electrolyte/solid interface.

Keywords: nitrogen reduction reaction, MVK mechanism, photoemission spectroscopy, electrocatalysis

(Some figures may appear in colour only in the online journal)

* Author to whom any correspondence should be addressed.

1. Introduction

1.1. Transition metal oxynitrides as nitrogen reduction reaction (NRR) catalysts

NH_3 is of critical importance for production of fertilizer for agriculture and is also of increasing interest as a hydrogen source for emerging energy applications (Humphreys *et al* 2020, Qing *et al* 2020). The commonly used Haber–Bosch process, run at high temperatures, now accounts for as much as 2% of the world's energy consumption, and (due to the use of fossil fuels) is a significant source of CO_2 (Humphreys *et al* 2020). The electrocatalytic NRR reaction is therefore of broad and increasing interest as an environmentally and energy-friendly alternative for NH_3 production. For a general survey of this area, the reader is referred to several recent reviews (Humphreys *et al* 2020, Qing *et al* 2020, Young *et al* 2022).

As a class of NRR electrocatalysts, transition metal oxynitrides are of significant interest (Yang *et al* 2018, 2019, Kang *et al* 2019, Young *et al* 2022). Du *et al* (2019) found that VN nanoparticles displayed significant NRR activity correlated with the formation of an oxynitride surface that included a N surface state characterized by a (*ex situ*) photoemission N1s binding energy of 396.5 eV. This contrasts with a binding energy of 397.1 for bulk lattice N and 400.5 eV assigned to surface $–NH_2$ groups induced by NH_3 plasma treatment (Osonkie *et al* 2020b). In contrast to V oxynitride, pure, O-free VN was found to be NRR inactive (Du *et al* 2019). Similarly, Kang *et al* (2019) found that TiN was NRR inactive, but that plasma oxidation produced a Ti oxynitride surface which was NRR active. These findings, together with the results of NRR experiments involving $^{15}N_2$ and yielding both $^{15}NH_3$ and $^{14}NH_3$, have led to the general acceptance of a Mars–van Krevelen (MVK) NRR mechanism for NRR reduction in these materials. In an MVK mechanism, N_2 is incorporated as N into the oxynitride lattice at N vacancy sites and subsequently reduced to NH_3 (Yang *et al* 2018).

The existence or non-existence of an MVK mechanism is not a superficial issue. This model also leads directly to the supposition that energetics for lattice N vacancy formation are essential for an effective NRR catalyst (Young *et al* 2022). The results discussed herein, however, suggest that indeed the opposite may be the case for some oxynitrides. If, as the evidence discussed below indicates, a principle effect of lattice N is stabilization of the metal cation in an intermediate oxidation state favorable for N≡N bond activation, and reduction of lattice N occurs without replacement by N_2, then favorable energetics for N vacancy formation could lead to the rapid transformation of the oxynitride to the corresponding—and less NRR active—oxide.

With respect to activating inactive metal nitrides for NRR, the effects of O-metal vs N-metal interactions, particularly with regard to metal oxophilicity (Moltved and Kepp 2019), are only beginning to be understood (Chukwunenye *et al* 2022). However, the results discussed herein indicate that the stabilization of the metal center in an intermediate oxidation state—e.g. V(III) vs V(IV)—is beneficial to enhance V/N_2 interaction.

The focus of this paper on V oxynitrides and oxides has been motivated by the generally high performance reported for such systems (Yang *et al* 2018, 2019). Indeed, certain publications report NH_3 production rates for V oxynitrides approaching or even exceeding thresholds proposed for commercial viability or targets set by the U.S. Dept. of Energy (Young *et al* 2022). A comparison to cobalt oxynitride (Chukwunenye *et al* 2022) affords a comparison of oxynitrides with high (V) and low (Co) oxophilicities (Moltved and Kepp 2019), and corresponding energies of N vacancy creation (Osonkie *et al* 2020a, Osonkie 2020b).

Theoretical and experimental studies of possible NRR reaction mechanisms (Hou *et al* 2020) have pointed to the possible general co-existence of the hydrogen evolution reaction (HER) and NRR. Such a general co-existence would, of course, detract from catalyst NRR efficiency and selectivity. As shown below, however, detailed studies show that V oxynitride is highly selective for NRR, at least at neutral pH. The results discussed herein also emphasize the importance of reaction conditions—particularly pH—in determining HER and NRR activities for a specific catalyst surface. In understanding the effects of reaction conditions, and other detailed aspects of surface chemistry, the role of theory is of great importance. This importance is enhanced by the challenges of applying conventional surface science methods—such as temperature programmed desorption and x-ray photoelectron spectroscopy (XPS)—to studies of the electrolyte/solid interface.

It must be emphasized that the focus of the studies reviewed here has been a fundamental understanding of transition metal oxynitride structure/function relationships, rather than optimization of catalyst performance. For this reason, there is an emphasis on surface analysis—including XPS—in concert with electrochemical methods and theory for understanding fundamental interface chemistry. Additionally, materials discussed herein have been in the form of thin films, rather than higher surface area nanorods, nanoparticles, etc. Challenges with respect to using XPS and preparing thin films in this context are discussed in the next section.

1.2. XPS and related methods at the electrolyte/solid interface

XPS and related surface science methods involving low energy ($<\sim$1000 eV) electron emission from the surface, such as Auger electron spectroscopy (AES), x-ray excited valence band spectroscopy, and ultraviolet photoelectron spectroscopy, have made enormous contributions to our understanding of heterogeneous catalysis at the vapor–solid interface (Sinfelt 2002, Somorjai and Li 2010, Kolasinski 2012). Electrons with these kinetic energies typically exhibit inelastic mean free paths $<\sim$50 nm through most solids, and are correspondingly surface sensitive (Briggs 1990). Since its development in the late 1960s and 1970s (Siegbah 1970) XPS—sometimes referred to as electron spectroscopy for chemical analysis—has become perhaps the most widely used and versatile technique for characterizing the chemical compositions and electronic structures of surfaces. A detailed

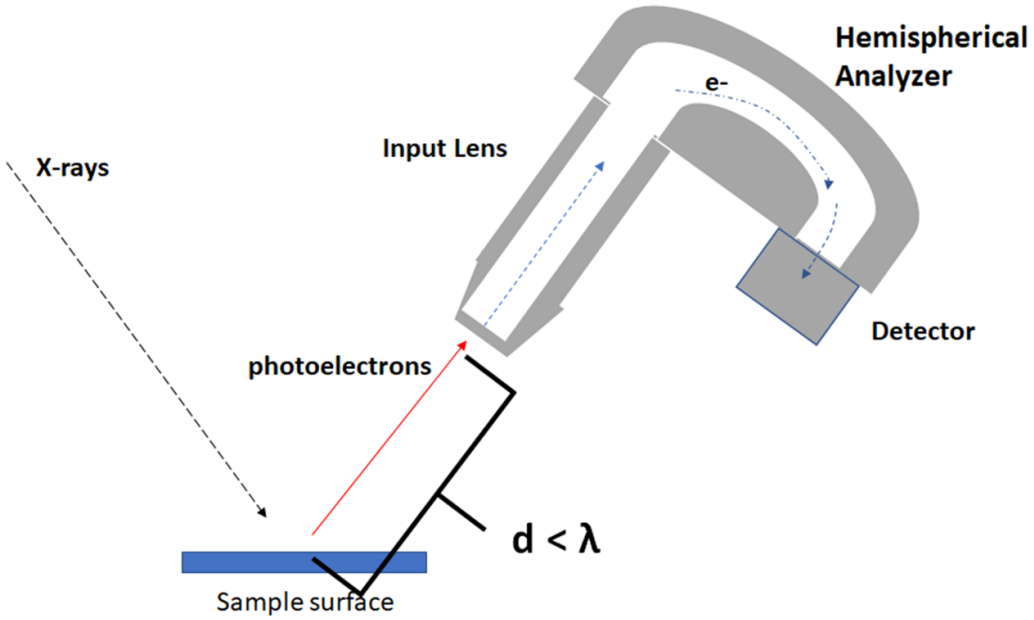

Figure 1. A central problem in XPS: the distance (d) that photoelectrons travel from the surface to the analyzer must be less than the inelastic mean free path (λ). For chamber pressures $\sim 10^{-8}$ Torr or less, $\lambda \sim 1$ m or more. For ambient pressure or liquids, $\lambda \sim 1$ μm or less.

explanation of XPS and related methods can be found elsewhere (Briggs and Seah 1990).

The early development of XPS occurred in parallel with the development of practical methods for obtaining and maintaining ultra-high vacuum (UHV), typically $<10^{-8}$ Torr. The chemical information of a photoelectron ejected by the photoelectric effect from the surface region under study is given by its kinetic energy (Briggs and Seah 1990). An inelastic collision between an electron and, e.g. a molecule in the gas or liquid phase, would remove all the chemical information from that photoelectron. The inelastic mean free path (λ) of a photoelectron with kinetic energy of 1000 eV (appropriate for laboratory photoemission studies) in UHV is on the order of meters (Kolasinski 2012). Thus, the maintenance of UHV conditions not only limits the flux of gas phase molecules to the surface, thus maintaining the chemical stability of the surface over the time of the experiment (often an hour or more), but also permits practical instrumentation for the detection of photoelectrons from the surface, with sample/analyzer distances easily less than λ (figure 1) (Briggs and Seah 1990, Kolasinski 2012). In contrast, inelastic mean free paths of photoelectrons with kinetic energies $\sim$1 keV or less (typical for laboratory x-ray sources) through ambient pressure gases or liquids are on the order of microns, or less (Kolasinski 2012), thus posing significant problems for experiments in that the distance between surface and detector would need to be significantly less than λ. This is the central problem in performing XPS at ambient pressures or at the liquid/solid interface, as illustrated in figure 1. For a more thorough explanation of this issue, specifically at the liquid–solid interface, the reader is referred to several sources in the literature (Emfietzoglou and Nikjoo 2007, Axnanda *et al* 2015).

Typically, such issues have been addressed by either *ex situ* or *in situ* photoemission, in which the sample is transferred from the reaction environment under ambient (*ex situ*) or controlled (*in situ*) conditions, the latter to avoid ambient-induced surface contamination. However, it has become apparent that in many circumstances, important surface chemistry is not accurately observed in UHV even with *in situ* methods. This is known as the 'pressure gap' in surface science, due to important surface species existing only in equilibrium with the gas phase (Freund *et al* 2001). This has stimulated the development of various *operando* methods for the study of such surfaces under realistic catalytic conditions, including high-pressure scanning tunneling microscopy (Jensen *et al* 1998), and sum-frequency generation (Su *et al* 1997). For a further description of available *operando* methods for surface characterization of complex structures, the reader is referred to a more recent publication (Eads *et al* 2020).

Several developments in XPS have addressed the pressure gap. In near ambient pressure XPS (NAP-XPS), differential pumping is used to limit the thickness of the high-pressure region above the surface to less than λ, permitting studies of surface species stable only in equilibrium with the gas phase (Salmeron and Schlögl 2008, Schnadt *et al* 2020). Studies at the liquid–solid interface have been addressed, beginning in the late 1980s, via the development of *in situ* sample transfer between electrolyte and UHV—sometimes termed 'UHV-electrochemistry' (UHV-EC) (Hubbard 1988, Soriaga 1992). Such methods, applied to the electrolyte/oxide or oxynitride interface, are discussed here. In addition, the application of NAP-XPS to the study of N_2-vanadium oxide interactions, and its possible relationship to electrolyte/oxide interactions, are also discussed.

The UHV-EC apparatus used in our laboratory is shown schematically in figure 2 and has been described in the literature (Kelber and Seshadri 2001). As shown, the sample comes in contact with the meniscus of the electrolyte in a

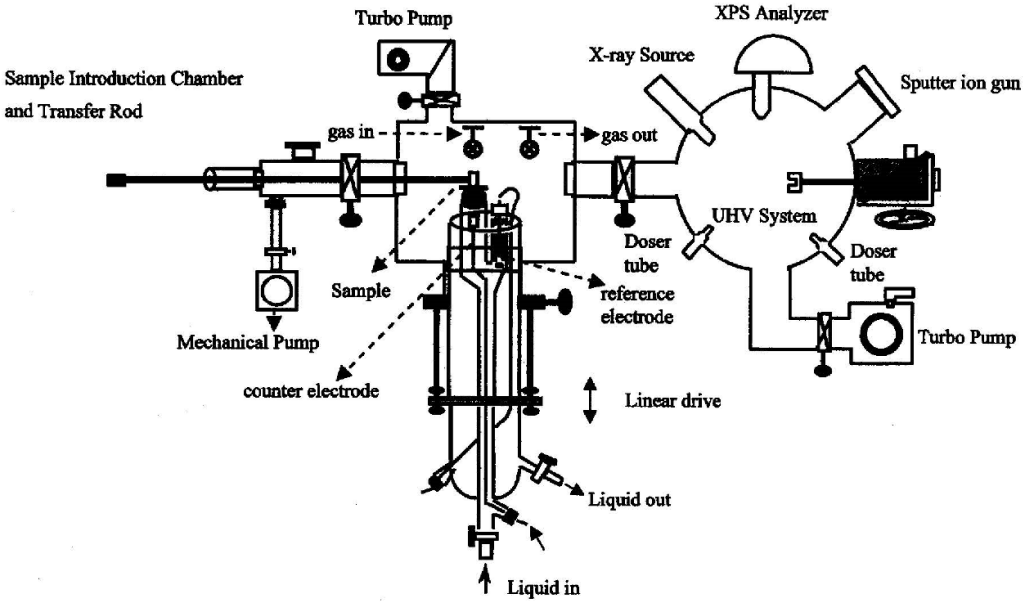

Figure 2. Schematic of UHV-EC apparatus. Kelber and Seshadri (2001) John Wiley & Sons. [Copyright © 2001 WILEY-VCH Verlag GmbH & Co. KGaA, Weinheim].

three-electrode cell. The sample is emmersed from electrolyte at controlled potential, then rinsed in de-ionized water to remove excess electrolyte, followed by a pump-down to vacuum and transfer to the UHV system for surface analysis. Reversal of this procedure can then bring a sample with a specific surface configuration into contact with the electrolyte (Kelber and Seshadri 2001).

As shown in figure 2, this method exhibits the virtue of simplicity, and the ability to track changes in surface composition induced by changes in electrolyte or potential, as described in the literature (Kelber and Seshadri 2001) and shown below. There are obvious weaknesses to this approach, however, including the necessity of rinsing in de-ionized water prior to transfer for analysis, and the unavoidable exposure of the sample to significant amounts of H_2O vapor during transfer to/from UHV. Thus, such an approach should not be regarded as providing a true *operando* insight into the electrolyte/solid interface.

Over the last 8–10 years, methods have also been developed for the *operando* XPS study of the electrolyte/solid interface. One approach, arguably still in the development phase, involves the drawing up of the sample from the electrolyte to generate a continuous liquid meniscus film. The film must be sufficiently thick and uniform, (∼20 nm or more) as to support an applied electrochemical potential (Ali-Löytty *et al* 2016). Here, the presence of water vapor and differential pumping are required to prevent film evaporation, as is the use of synchrotron radiation to generate photoelectrons of sufficient kinetic energies that the inelastic mean free paths are longer than the film thickness, or region of high-pressure water vapor (Axnanda *et al* 2015, Ali-Löytty *et al* 2106). Alternative electrochemical cell designs for *operando* XPS studies have recently been discussed (Velasco-Vélez *et al* 2021). *Operando* XPS studies at the electrolyte/solid interface have not yet been incorporated as part of this NRR effort, but are being contemplated for future experiments.

1.3. Thin film deposition and characterization

The studies reviewed here have used films deposited by DC magnetron sputter deposition, as discussed below. Magnetron sputtering is a well-studied method of thin film deposition. Details can be found in the literature (Kelly and Arnell 2000, Padhan *et al* 2018). Transition metal oxide and oxynitride surfaces discussed herein were prepared by DC Magnetron Sputter Deposition, in the system shown schematically in figure 3. This system permits sample heating between ∼300 K and 1000 K, with *in situ* sample transfer between sputter deposition chambers and surface characterization chamber. The latter contains a commercial single pass cylindrical mirror analyzer with co-axial electron gun (Staib Instruments) for AES and reflective electron energy loss spectroscopy.

Vanadium oxide films were produced by DC sputter deposition of a V metal film onto a fluorinated tin oxide (FTO) substrate (for electrochemistry studies) or a Ta substrate (for NAP-XPS studies), with substrates first cleaned by annealing in O_2 to remove adventitious carbon (Ganesan *et al* 2021, Balogun *et al* 2022). DC sputtering conditions were 4 mTorr Ar at 25 W for ∼7 min deposition time, producing films with estimated thicknesses >30 nm (Ganesan *et al* 2021, Balogun *et al* 2022). Films were subsequently oxidized to produce V oxide films, using a custom-built inductively coupled plasma source and an O_2 plasma (20 W, 40 mTorr O_2) (Ganesan *et al* 2021).

Vanadium oxynitride (VO_xN_y) films were produced on FTO substrates, using DC sputter deposition with mixed $N_2 + O_2$ plasmas at a total gas pressure of 4 mTorr, 25 W, for 7 min. Variation of the N_2/O_2 partial pressure ratio yielded

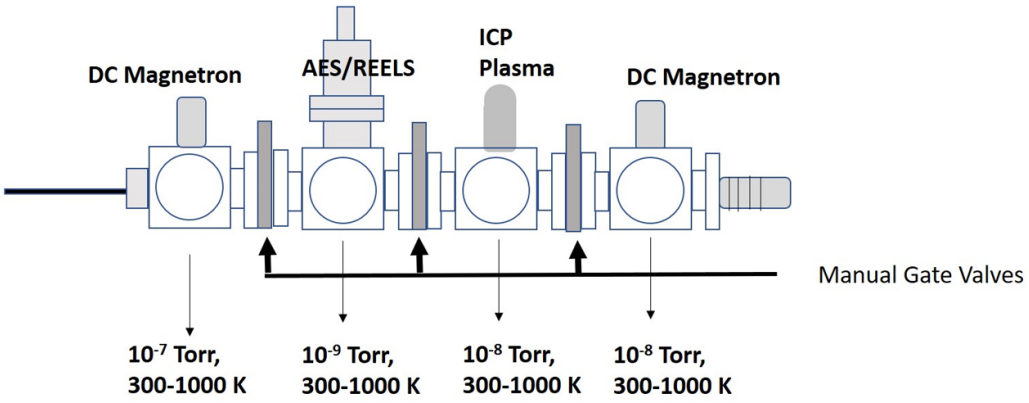

Figure 3. Schematic of system for DC magnetron sputter deposition and *in-situ* auger and electron energy loss analysis.

corresponding changes to N/O atomic ratio in the vanadium oxynitride film, as measured by *in situ* AES. Optical microscopy, atomic force microscope (AFM) and x-ray diffraction (XRD) measurements indicated such films to be polycrystalline, with an root mean square (RMS) roughness of ∼36 nm, conformal to the FTO substrate (Osonkie *et al* 2022). Vanadium oxynitride films of similar topography and composition were also produced by sputter deposition in an Ar:N_2 (1:4) plasma with a total pressure of 4 mTorr, 25 W (Chukwunenye *et al* 2022).

Cobalt oxynitride films were also produced using Ar:N_2 plasmas for DC sputter deposition (Chukwunenye *et al* 2022). Although *in situ* AES immediately after sputter deposition showed only Co and N, subsequent exposure to ambient and *ex-situ* XPS analysis showed the presence of a cobalt oxynitride surface region (Chukwunenye *et al* 2022).

2. Results

In this section, results are summarized for studies of V and Co oxynitrides and oxides with respect to (a) the roles or lattice N and lattice O interactions in NRR activity, and the non-existence of an MVK mechanism for these materials; (b) the roles of V(III) vs. V(IV) oxidation states in N_2 binding; and (c) catalyst selectivity for NRR vs HER.

2.1. Lattice N and O interactions and NRR

2.1.1. Lattice N and surface N states. Pioneering work by Yang and co-workers (Yang *et al* 2018, 2019) demonstrated that NRR activity in VN nanoparticles was associated with the formation of a V oxynitride surface, and specifically with the relative intensity of an N state characterized by an N1s XPS binding energy of 396.5 eV. Subsequent XPS studies of V oxynitride films deposited by magnetron sputter deposition, combined with DFT-based theoretical calculations (Osonkie *et al* 2020a), demonstrated that this N1s feature did *not* correspond to a lattice N state within the oxynitride (figure 4(a)). Such a lattice N state is characterized by an N1s binding energy of 397.1 eV (figures 4(a) and 5) (Osonkie *et al* 2020a, 2022). Instead, experiment and theory indicate that the N1s binding energy of 396.5 eV is attributable to an unsaturated N surface state that could be induced by, e.g. O_2 plasma oxidation of V oxynitride, as shown in figure 4(c), but not by thermal oxidation (Osonkie *et al* 2020a). The intensity of this N surface state could also be reduced by annealing in UHV (Osonkie *et al* 2020a). Corresponding DFT-based calculations indicate that the N1s feature at 396.5 eV indeed corresponds to an unsaturated V–N surface state, likely V≡N, as illustrated in figure 4 (Osonkie *et al* 2020a).

The specific identification of the intensity of the N1s feature at 396.5 eV with NRR activity (Yang 2018) and with an unsaturated surface state (figure 5) rather than with a regular lattice state, strongly suggests that this state corresponds to a reaction intermediate in the NRR reduction reaction, e.g.,

$$\mathrm{V-N\equiv N:} \rightarrow \mathrm{V\equiv N:} \; + \tfrac{1}{2}\,\mathrm{N_2}. \qquad (1)$$

The formation of such a N surface state, with a binding energy of 396.5 eV, is observed after cathodic polarization of a V oxynitride film in both Ar-saturated and N_2-saturated Na_2SO_4 electrolyte (pH 7), as shown in figure 6 for N_2-saturated electrolyte (Osonkie *et al* 2022). The appearance of the N1s feature at 396.5 eV binding energy, after both O_2 plasma oxidation and electrochemical oxidation in the absence of N_2, (Osonkie *et al* 2020a, 2022) indicates that this N surface state is produced by a process other than, or in addition to, N_2 dissociation at V surface sites. Importantly, however, lattice N is reduced to NH_3 even in the absence of N_2, as discussed below (Osonkie *et al* 2022). Therefore, the data are consistent with the V≡N: surface state at a binding energy of 396.5 eV being an intermediate in the electrochemical reduction of lattice N to NH_3.

The data in figures 4–6 demonstrate that cathodic polarization transforms lattice N into a V≡N: surface state, consistent with this state being an intermediate in the formation of NH_3, and with the existence of an MVK mechanism. Electrochemical and absorption measurements also demonstrate that, in the absence of N_2, lattice N in vanadium oxynitride is reduced to NH_3, as demonstrated in figure 7 (Osonkie *et al* 2022). Also consistent with this is the fact that the production of NH_3 in the absence of N_2 coincides with the depletion of lattice N within the XPS sampling depth, as determined by *ex situ* XPS (Osonkie *et al* 2022).

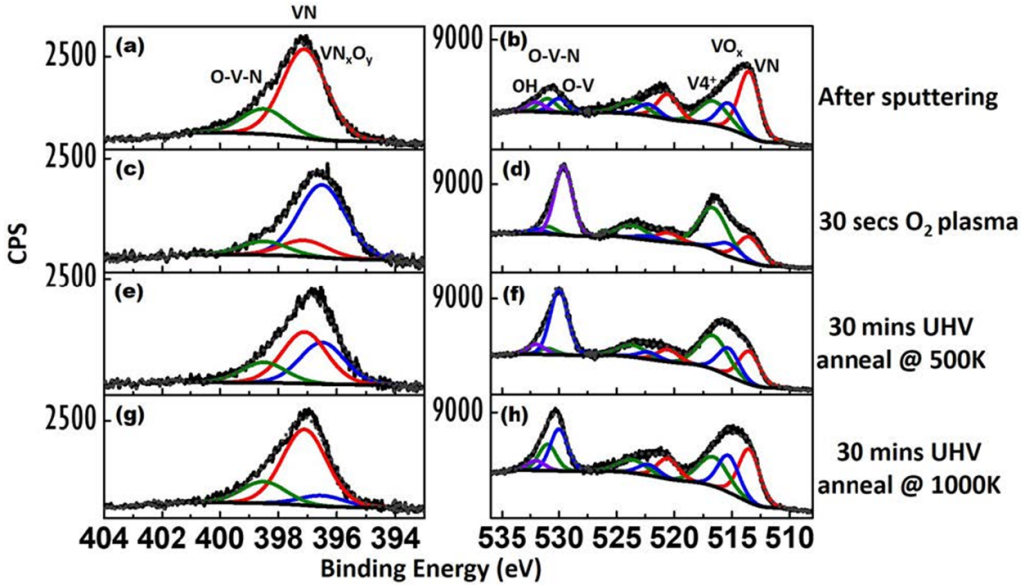

Figure 4. XPS data [(a) and (b)] of N1s and O1s/V2p, respectively, after extensive sputtering in UHV ($VO_{0.4}N_{0.6}$); [(c) and (d)] corresponding data after 30 s O_2 plasma treatment ($VO_{0.7}N_{0.3}$); [(e) and (f)] corresponding data after 30 min anneal to 500 K in UHV ($VO_{0.7}N_{0.3}$); and [(g) and (h)] corresponding data after an additional 30 min anneal to 1000 K in UHV ($VO_{0.6}N_{0.4}$). Film compositions given in parentheses are based on total O1s and N1s intensities. Reprinted from Osonkie *et al* (2020), with the permission of AIP Publishing.

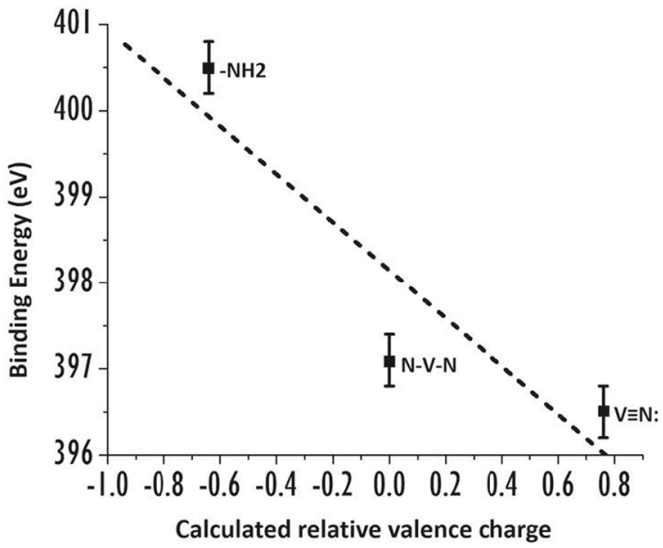

Figure 5. Experimental N1s binding energies vs. DFT-calculated N valence charge densities (relative to N−−V−−N lattice sites) for V−−NH_2 and V≡N: surface configurations. The dashed line is least squares fit to the data. The V=NH feature is not shown due to its near coincidence with the valence charge density of the N−−V—N surface configuration, Reprinted from (Osonkie *et al* 2020a), with the permission of AIP Publishing.

Inconsistent with an MVK mechanism, however, are the observations that (a) lattice N depletion is observed even in an N_2-saturated solution (Osonkie *et al* 2022), and that N-free vanadium oxide is also NRR active under similar conditions (pH 7), without any observation of incorporation of N into the lattice (Ganesan *et al* 2021). It should be noted that the reduction of both lattice N and N_2 by parallel but distinct reaction mechanisms, rather than by a coupled MVK mechanism, would account for the findings of both $^{15}NH_3$ and $^{14}NH_3$ being produced by the reduction of $^{15}N_2$ (Yang *et al* 2019). Therefore, we conclude that, with respect to V oxynitride, N_2 and lattice N are reduced to NH_3 by separate mechanisms, and that the existence of an MVK mechanism is not supported by the evidence.

The non-existence of an MVK mechanism for V oxynitride, combined with a separate mechanism for lattice N reduction, implies that V oxynitride catalysts will, eventually, be depleted of lattice N, an observation consistent with previous reports in the literature (Yang *et al* 2018). As N-free V oxides are also NRR active at pH 7 (Ganesan *et al* 2021), while O-free VN and other metal nitrides are NRR inactive (Du *et al* 2019), the role of lattice O in NRR active metal oxides and oxynitrides warrants further consideration.

2.1.2. Lattice O. As O-free VN and other oxygen-free transition metal nitrides are NRR inactive (Du *et al* 2019), the impact of lattice O on the NRR process is obviously significant and needs to be examined in some detail. This is demonstrated in figure 8, which provides a direct comparison of the electrochemical behavior (figure 8(a)) and indophenol blue absorption due to NH_3 production (figure 8(b)) for both an N-free V oxide film and a V oxynitride film under identical reaction conditions—pH 7, 0.1 M Na_2SO_4 (Osonkie *et al* 2022). The V oxide data in figure 8 for sputter-deposited V oxide are very similar to those reported previously (Ganesan *et al* 2021). The data in figure 8 show that both N-free V oxide and V oxynitride display similar electrochemical behavior. There is a slight relative increase in NH_3 production for the oxynitride (figure 8(b)). This, and the somewhat different current magnitudes and threshold potentials suggest that (a) in addition to NRR, somewhat different electrochemical reactions

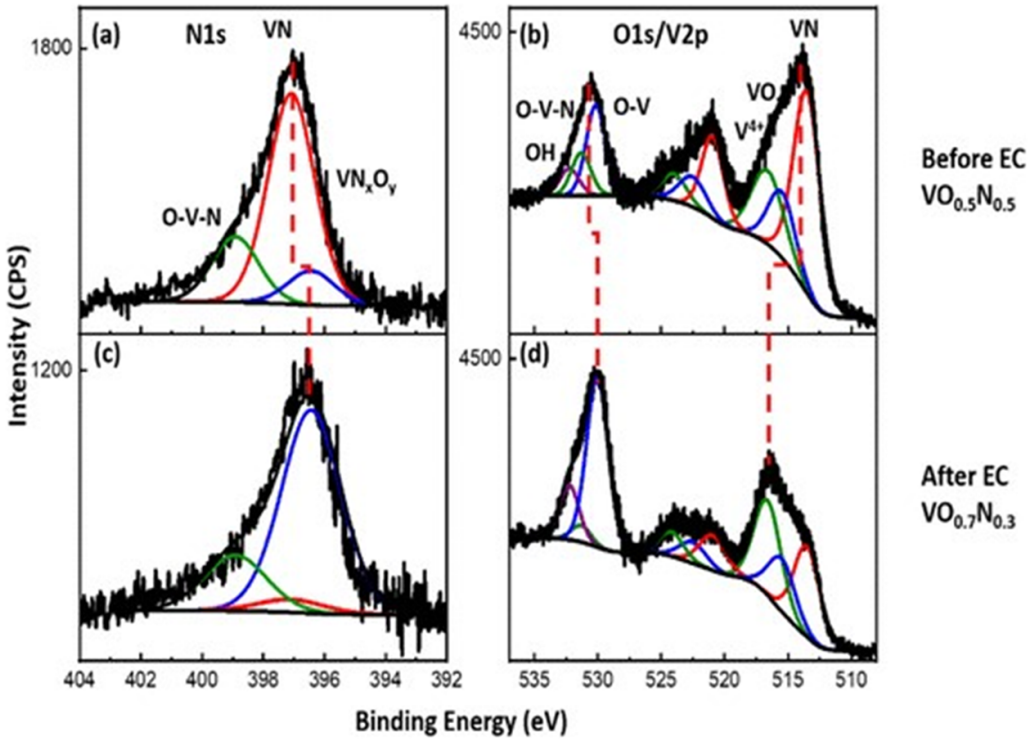

Figure 6. (a) N1s and (b) O1s/V2p spectra for a $VO_{0.5}N_{0.5}$ film after deposition but prior to electrochemical measurements: (c) and (d); corresponding data after emersion from the N_2-saturated Na2SO4 electrolyte (pH = 7) at −1.6 V vs. Ag/AgCl. Dashed lines are guide to the eye. Reprinted with permission from Osonkie *et al* (2022). Copyright (2022) American Chemical Society.

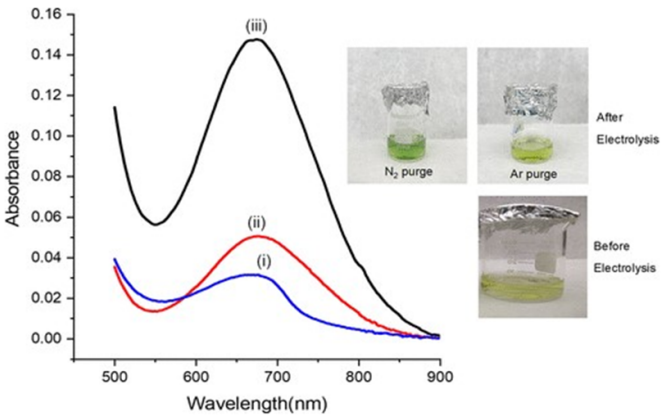

Figure 7. Absorbance spectrum (i) prior to electrolysis of blank solution, (ii) after electrochemical polarization of a $VO_{0.7}N_{0.3}$ film in the Ar-saturated solution, and (iii) after electrochemical polarization of a $VO_{0.7}N_{0.3}$ film in the N_2-saturated solution. Electrolysis was performed in 0.1 M Na_2SO_4 (pH 7). The Ar and N purge times were both 10 min. The run time was 90 min at −0.7 eV vs. Ag/AgCl. Reprinted with permission from Osonkie *et al* (2022). Copyright (2022) American Chemical Society.

may be occurring at the oxide and oxynitride surfaces, and (b) that the somewhat higher NH_3 production in the oxynitride is consistent with the simultaneous reduction of both lattice N and N_2 at the oxynitride surface. The greater current and different threshold potential for the oxide (figure 8(a)) may reflect HER activity in the oxide and not the oxynitride (but see below).

DFT-based calculations indicate that for metals of high oxophilicity (Moltved and Kepp 2019), the dissociation of adsorbed N_2 to V≡N:, a plausible reaction intermediate (equation (1)), is significantly energetically favored at a surface V site bonded to 5 oxygen ligands, compared to surface V bonded to 5 N ligands in the rocksalt structure (figure 9) (Ganesan *et al* 2021). Extension of these calculations to other oxides indicates a similar trend for Ti and V, but not for Cr (figure 10) (Ganesan *et al* 2021). It is thus apparent that the role of lattice O in the V oxynitride—and possibly other oxophilic metal—is to enhance N_2 binding/dissociation at the metal cation site.

The above results demonstrate that the role of lattice O in V oxynitride is critical to N_2 reduction. These findings also provide an explanation for observed NRR inactivity of O-free VN (Du *et al* 2019), as well as the NRR activity of N-free V oxide (Ganesan *et al* 2021). Furthermore, the observed lack of an MVK mechanism means that any enhanced NRR activity due to the presence of lattice N will eventually degrade as the lattice N becomes depleted. However, V oxides may display a broad variety of oxidation states, even within a single thin film or nanostructure (Biesinger *et al* 2010, Goodacre *et al* 2020).

It is therefore fair to ask what V oxidation state (or states) is (are) most favorable for N_2 binding/reaction. This issue is explored in the next section.

2.2. *The V oxidation state*

A key issue in the use of metal oxynitrides as NRR electrocatalysts is the role of metal cation d electrons in N≡N

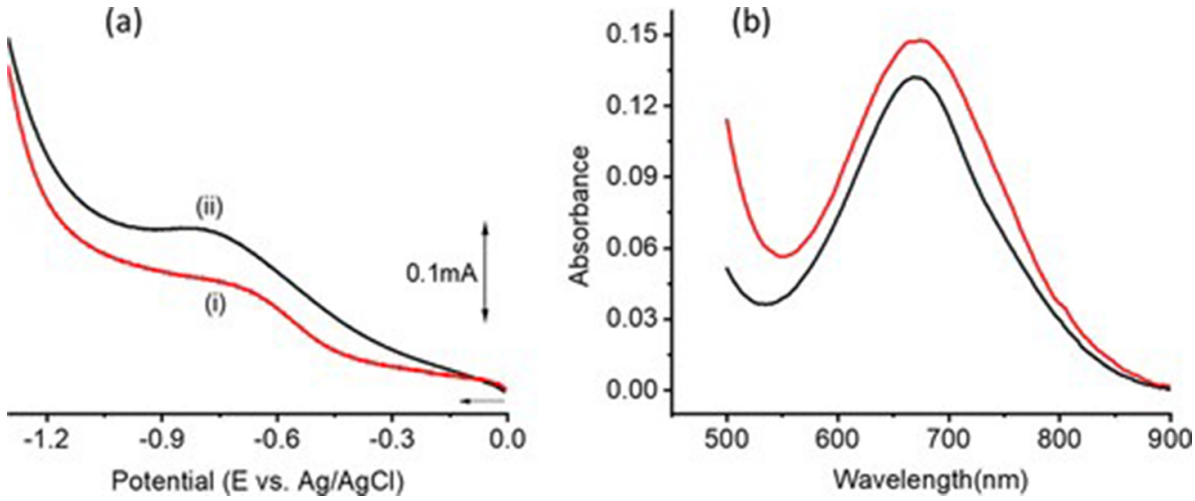

Figure 8. (a) Comparison of EC polarization curves for the (i) $VO_{0.4}N_{0.6}$ film on FTO (red trace) and (ii) N-free VO_x film on FTO (black trace) in N_2-saturated 0.1 M Na_2SO_4 at pH 7. (b) Absorbance spectrum of indophenol blue from NH_3 produced by controlled potential bulk electrolysis of the (i) $VO_{0.4}N_{0.6}$ film (black trace) and (ii) N-free VO_x film (red trace). Reprinted with permission from Osonkie *et al* (2022). Copyright (2022) American Chemical Society.

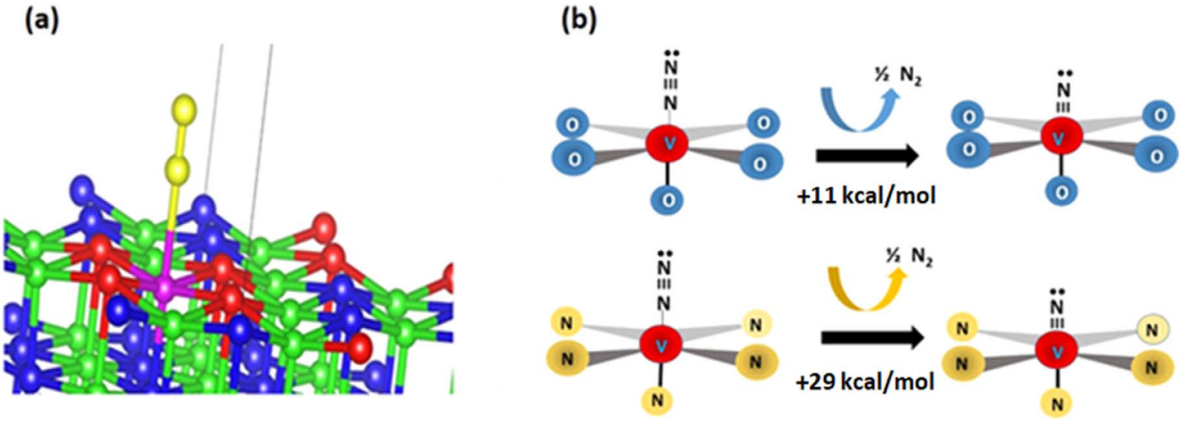

Figure 9. Portion of DFT-optimized surface unit cell for $[V]_O$–N_2 model. Colors: V to which N_2 is coordinated = magenta; other V = green; nitrogen atoms of N_2 = yellow; other N = blue; surface O = red. In $[V]_N$–N_2 model, surface O are replaced with N then re-optimized. From these were generated $[V]_{N,O} \equiv N$: models by removal of the terminal N of N_2, and $[V]_{N,O}$ models by removal of both nitrogen atoms of N_2. After each change to the surface, the model was re-optimized with DFT methods. (b) Computational results showing reaction energetics N_2 scission on O-supported V surface sites are substantially lower than on N-supported sites. © 2021 Ganesan *et al* (2021). Published on behalf of The Electrochemical Society by IOP Publishing Limited.

bond activation. This is illustrated by the results of DFT-based calculations (figure 11), showing calculated N≡N stretching frequency (*y*-axis) vs N≡N bond distance (*x*-axis) for N_2 bonded end-on to selected metal centers in various oxidation states. Calculations were performed on molecular models of N-rich (ligated amide, NH_2) and O-rich (ligated by hydroxide, OH) vanadium-dinitrogen surface configurations of varying d-count on the metal. To assign the formal oxidation state of the metal and hence d-count typical electron counting rules were employed, i.e. amide and hydroxide $=1-$ charge. The Gaussian 16 code (Gaussian 16, Revision C.01, Frisch *et al* 2016) was used for these simulations and the level of theory employed was the B3LYP functional (Vosko *et al* 1980, Lee *et al* 1988, Becke 1997) in conjunction with the def2-svp basis set (Weigend and Ahlrichs 2005). Continuum solvent effects were modeled via the solvent model density (SMD) solvation method (Marenich *et al* 2009), assuming water as the solvent. Various low-, intermediate- and high-spin states were evaluated, and the reported data are for the most stable spin state. For all open-shell entities (multiplicity >1), the unrestricted Kohn–Sham formalism (Kohn and Sham 1965) was employed. For all stationary points, vibrational spectra were computed.

Notably, the data in figure 11 show that, in general, a metal (+3) oxidation state provides enhanced bond activation relative to the corresponding (+4) oxidation state for the transition metals considered. Indeed, the calculations in figure 11 indicate that V(IV) will not even bind N_2, although V(III) will. In essence, the results in figure 11 indicate that the stabilization of transition metal centers in *intermediate* oxidation states is beneficial to N≡N bond activation and NRR. Indeed, the XPS data in figure 6 suggest that reduction of lattice N via the formation of a V≡N: surface state is coupled with further oxidation

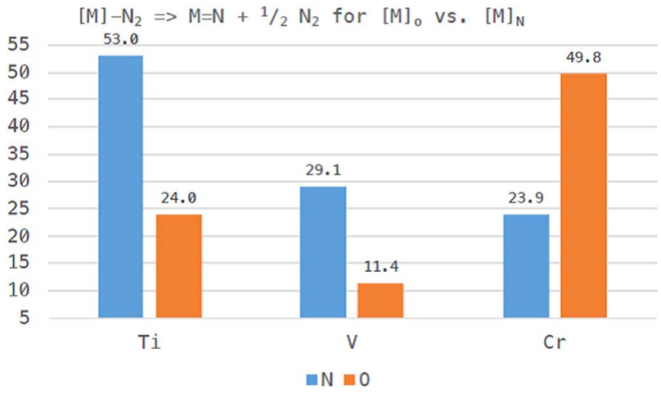

Figure 10. Energetics (in kcal mol^{-1}) for N_2 scission on metal-oxynitride (rock salt structure; 100 surface) surface sites ([M]–N_2) → [M] ≡ N: $+^1/_2N_2$, for M = Ti, V and Cr.

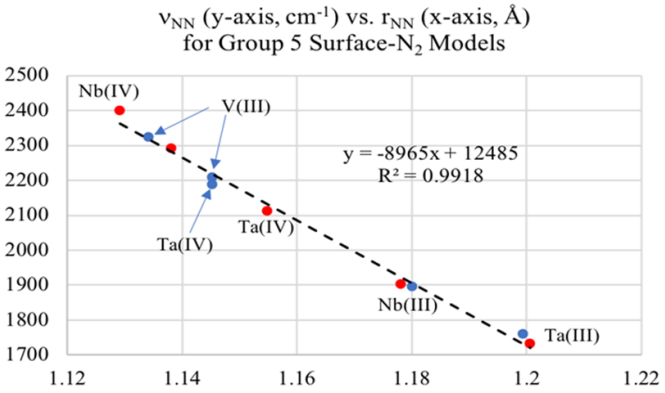

Figure 11. PBE0/CEP-31 G(d) calculated NN stretching frequency (*y*-axis, cm^{-1}) versus calculated NN bond distance (*x*-axis, Å) for 3+ and 4+ formal oxidation state Group 5 (V, Nb, Ta) oxynitride surface-bound N_2 models. O- and N-supported surface configurations are denoted by red and blue circles, respectively. Activation of N_2 is generally greater for Ta > Nb > V, and for 3+ than 4+ surface sites; relative activation of N_2 by N- vs. O-supported sites is metal dependent.

of the V site. Therefore, understanding the interaction of N_2 with V(III) vs. V(IV) (or V(V)) is important to a fundamental understanding of the functioning of V oxynitride, and other oxynitrides, as NRR catalysts.

To address the above question, NAP-XPS studies were carried out at room temperature on a V oxide surface with a distribution of V oxidation states, mainly V(IV), but including V(V) and a small proportion of V(III) (Balogun *et al* 2022). Studies were carried out at the Advanced Light Source (ALS) on V oxide films fabricated at UNT, and then cleaned off surface C and other contaminants at ALS. Vanadium O1s/V2p core level spectra are displayed in figure 12. Using the V oxidation state calibration method reported by Goodacre and co-workers (Goodacre *et al* 2020) and based on earlier work (Coulston *et al* 1996), the data show that the average V oxidation state is between V(IV) and V(V), although a minority of V(III) states is present (Balogun *et al* 2022).

NAP-XPS core level spectra of N_2 on this V oxide surface are shown in figure 13. N1s spectra (figure 13(a)), acquired at N_2 pressures up to 10^{-1} Torr show that the N1s spectrum of species bound to the surface (i.e. excluding the spectrum of gas-phase N_2)—is observable at pressures $>10^{-5}$ Torr, and consists of a broad feature centered at a binding energy of 401.0 eV, and a less intense feature centered near 398.7 eV (Balogun *et al* 2022). N/surface binding is sufficiently strong that the N1s spectrum observed at 10^{-1} Torr (figure 13(a)) is essentially unchanged upon pump-down to UHV. As shown in figure 13(b), O1s and V2p core level spectra are also unchanged upon exposure to N_2 at room temperature. Exposures of the same surface to equal partial pressures of N_2 and H_2O up to 10^{-1} Torr result in a significant but not complete decrease of N1s intensity, with no observable change in N1s binding energies.

Given the data in figures 12(b) and 13(b), indicating that the prevalent V oxidation state in the surface region is V(IV), one might conclude that the XPS data in figure 13 represent binding to the majority V(IV) sites in the vanadium oxide film. However, the total N1s intensity indicates that the maximum amount of N adsorbed corresponds to $\sim 1.5 \times 10^{13}$ atoms cm^{-2}—a very small fraction of a monolayer (Balogun *et al* 2022). Additionally, DFT-based calculations of N_2 binding to various V oxide structures with V in different oxidation states (table 1) indicate significant N_2 absorption energies at V(III) and various V(IV) sites. However, only at V(III) sites does the calculated absorption energy for N_2 exceed that calculated for H_2O, consistent with the N_2/H_2O co-adsorption data (see (Balogun *et al* 2022)).

Hartree–Fock self-consistent field calculations of the photoemission process for N_2 bound end-on to V sites surrounded by point charges indicate that the N1s spectral features centered at 401.0 eV and 398.7 eV (figure 13) can be accounted for as the shakeup and normal 1s excitation features, respectively, for N_2 bound to V(III), but not to V(IV). A part of the high binding energy spectral weight in N1s spectra can also be also ascribed to a different adsorption site or to a dissociative adsorption. For the shake-up energy as shown in figure 14, the energy separation between the shakeup and normal features is calculated to be 3.3 eV, in reasonable agreement with an experimental value of 2.3 eV (figure 13(a)). However, the calculated shakeup-normal energy separation for N_2 bound to V(IV) is ∼13 eV. Thus, experimental N1s intensities, calculated N_2 adsorption energies, and detailed calculations of shake and normal N1s excitation energies are all consistent with N_2 interacting with V(III), rather than V(IV) sites. (Possible interactions with V(V) sites were excluded on the basis of calculated N_2 adsorption energies, as shown in table 1) (Balogun *et al* 2022).

The above findings regarding the NAP-XPS study are certainly consistent with the calculations shown in figure 11—that N_2 binds strongly to V(III) sites, but not to V(IV). However, one must then ask how representative the V2p spectra shown in figure 13(b) are of a V surface in an aqueous electrolyte under NRR conditions. To address this issue, UHV-EC data were acquired for a

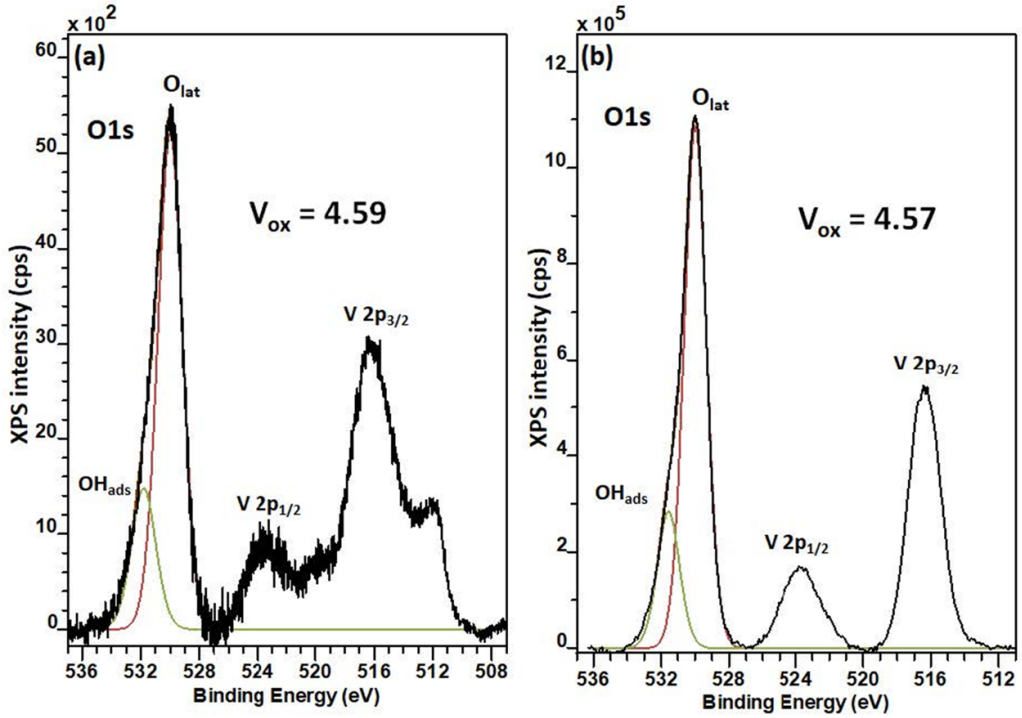

Figure 12. XPS O1s/V2p spectra of the vanadium oxide film (a) acquired after plasma oxidation at the UNT, and (b) immediately prior to initial N_2 exposure at the ALS. Average V oxidation states (V_{ox}) are shown. Reprinted from Balogun *et al* (2022), with the permission of AIP Publishing.

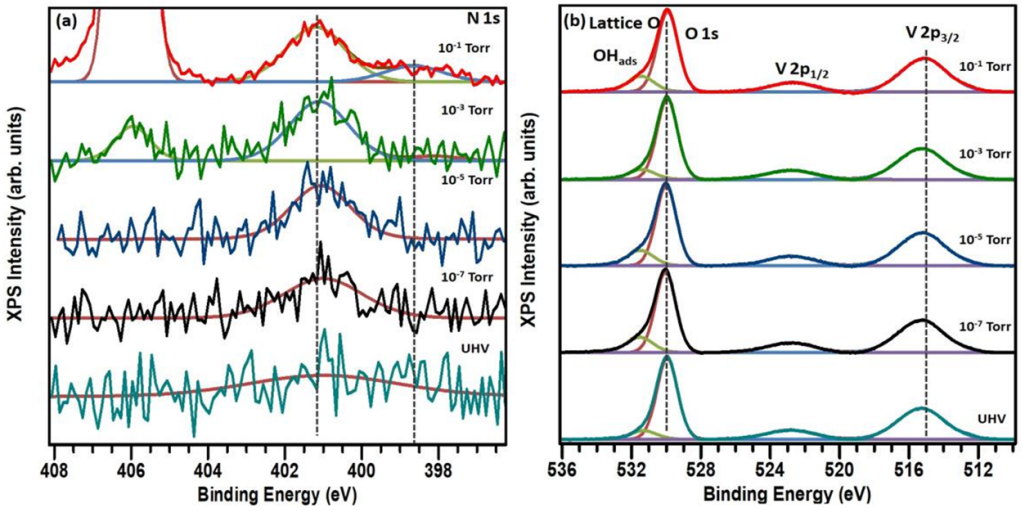

Figure 13. N1s (a) and (b) O1s/V2p spectra as a function of N_2 pressures between 10^{-7} and 10^{-1} Torr and ambient temperature. The O1s spectrum has been deconvoluted into components representing adsorbed OH and lattice O (OH_{ads} and O_{lat}) on the basis of previous studies. Dashed lines are guides to the eye. Reprinted from Balogun *et al* (2022), with the permission of AIP Publishing.

V oxide film—similar to the one used in the NAP-XPS studies—in a 0.1 M Na_2SO_4 electrolyte (pH 7), as shown in figure 15.

The UHV-EC data in figure 15 show that, in agreement with the V Pourbaix diagram (Lee *et al* 2020), a V oxide surface with an average oxidation state near 4.0 would, upon immersion, undergo significant reduction, yielding a hydroxylated surface with an average V oxidation state <4.0, indicating an increase in V(III) oxidation sites in the surface region. As expected, cathodic polarization to typical NRR potentials yields oxidation. Thus, the data in figure 15, together with the calculations summarized in figure 11, and the NAP-XPS findings summarized here, strongly suggest that V oxide films would be significantly more active for NRR if V centers could be stabilized in V(III) oxidation states under reaction conditions, Indeed XPS data for V oxynitrides (Osonkie *et al* 2020a, 2022)—e.g. figure 6—demonstrate that the presence of lattice N does yield an average V oxidation state closer to V(III).

Table 1. Comparison of calculated N_2 and H_2O absorption energies (AE) and exchange energies [E-exch = AE(H_2O) − AE(N_2)]. Energies are calculated for N_2-end on bonding to the V cation site. V–N and N–N bond lengths [r(VN)] and r(NN) are also given as is the V–O bond length trans to N_2–V interaction. Bond energies are in eV. Bond lengths are in Å. Reprinted from Balogun *et al* (2022), with the permission of AIP Publishing.

Oxide	Morph	Face	CN(V)	Geom	f.o.s.	AE(N_2)	AE(OH_2)	E-exch	r(VN)	r(NN)	Trans VO
VO	r.s.	001	6	Oh	II	−0.81	−0.96	−0.15	1.967	1.133	2.445
V_2O_3	R3-c	0001	4	Td	III	−0.64	−0.19	0.45	1.947	1.136	n/a
VO_2	Rutile	111	6	Oh	IV	−0.44	−0.66	−0.23	2.118	1.113	2.014
VO_2	Rutile	110	'6'	SQP5	IV	−0.83	−1.29	−0.46	1.989	1.127	2.801
VO_2	C2m	100	3	TP3	IV	−0.95	−0.98	−0.03	1.973	1.137	n/a
V_2O_5	Pmmn	010	6	Oh	V	−0.17	−0.42	−0.25	2.869	1.108	1.609

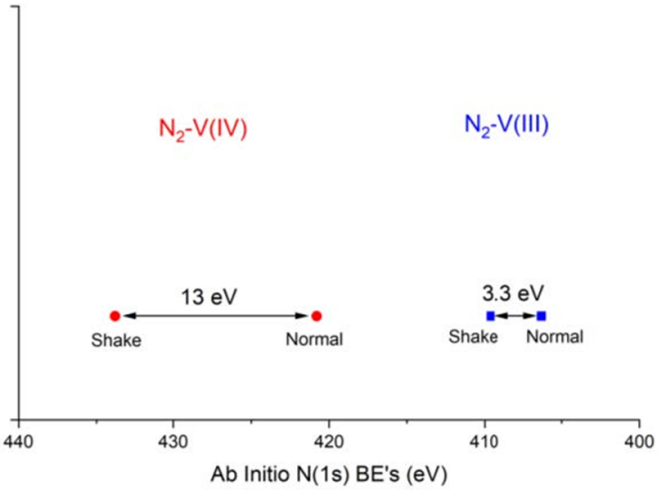

Figure 14. Schematic summary of calculated binding energies and splitting between shake and normal (Koopmans') N1s excitations for (right) N_2 bonded end-on to V(III) site and (left) to a V(IV) site. Reprinted from Balogun *et al* (2022), with the permission of AIP Publishing.

Thus, the relatively high NRR activities reported for V oxynitrides (Humphreys *et al* 2020) are consistent, not just with lattice N as an additional source of NH_3, but also with enhanced N_2 binding/activation at V(III) sites. The Pourbaix diagram for V (Lee *et al* 2020) suggests that this should be the case at pH 7 and under acidic conditions, at which V oxynitride NRR activity has been reported (Yang *et al* 2018, 2019, Osonkie *et al* 2022).

2.3. Catalyst selectivity: NRR vs. HER

Catalyst selectivity for NRR over HER is an important consideration in optimizing catalyst production and reaction conditions for actual use, as significant HER production obviously lowers the rate of ammonia production (Pan *et al* 2020, Qing *et al* 2020). We have used gas chromatography-mass spectrometry (GC-MS) to compare NRR and HER production for V oxynitride at pH 7 and pH 10, and for Co oxynitride a pH 10 (due to film electrochemical instability at pH 7) (Chukwunenye *et al* 2022). Notably, V oxynitride is NRR active at pH 7, and NRR inactive at pH 10, while Co oxynitride is NRR active at pH 10 (Chukwunenye *et al* 2022).

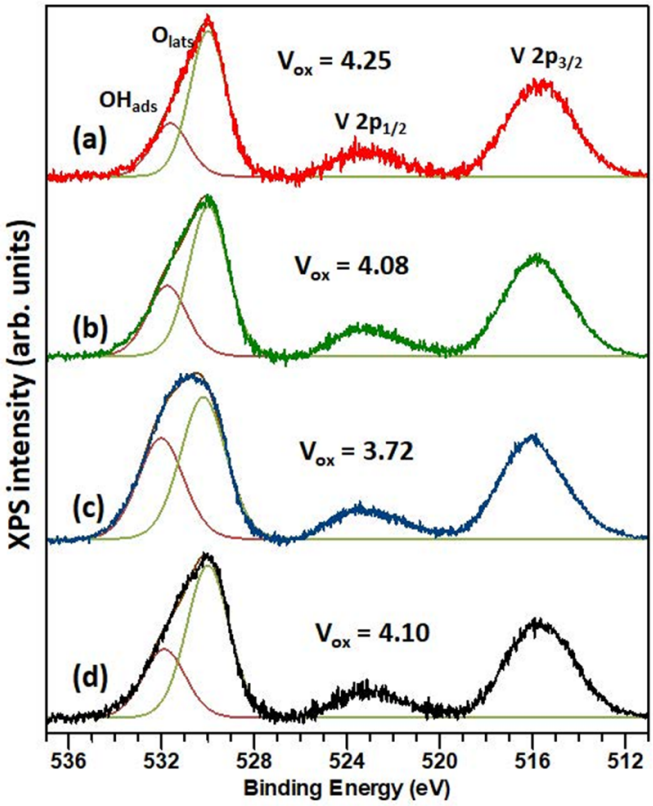

Figure 15. UHV-EC XPS spectra for a V oxide film prepared by MBE: (a) after ambient exposure and subsequent Ar ion sputtering to remove adventitious C; (b) after immersion in de-ionized water at open circuit potential; (c) after immersion at open circuit potential in 0.1 M Na_2SO_4, emersion, and rinsing in de-ionized water; and (d) after Ar ion sputtering and immersion in 0.1 M Na_2SO_4 and polarization to and emersion at −0.8 V vs Ag/AgCl, followed by rinsing in de-ionized water. Average V oxidation states (V_{ox}) are shown. Reprinted from Balogun *et al* (2022), with the permission of AIP Publishing.

GC-MS data for H_2 evolution, summarized in figure 16, show that V oxynitride is HER inactive at pH 7, whereas Co oxynitride is HER active at pH 10. The data thus demonstrate the high selectivity of V oxynitride at pH 7.

DFT calculations indicate that an important reason for this difference in NRR selectivity between V and Co oxynitrides is the reactivity of H_2O at the metal cation site. These calculations indicate far more favorable reaction energies (by >1 eV)

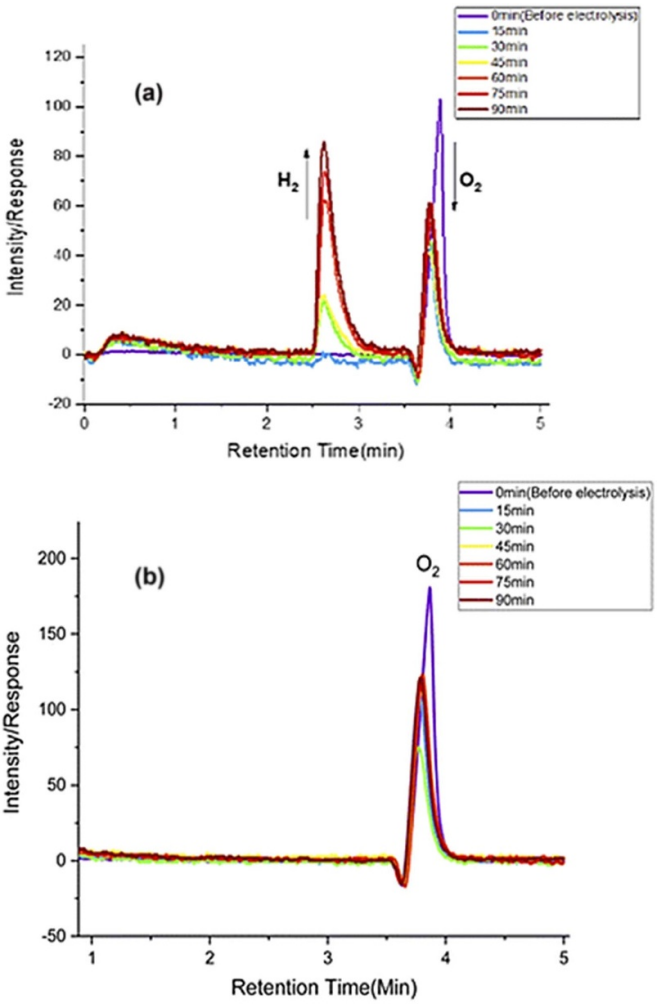

Figure 16. GC mass spectrometry data for H_2 evolution from (a) $CoO_{0.8}N_{0.2}$ at pH 10 and (b) $VO_{0.4}N_{0.6}$ at pH 7. Reproduced from Chukwunenye *et al* (2022) with permission from the Royal Society of Chemistry.

for O–H bond scission of adsorbed H_2O at Co vs metal cation site (equation (2)), leading to H_2 formation:

$$H_2O_{(ads)} \rightarrow OH_{(ads)} + H_{(ads)} \qquad (2a)$$

$$H_{ads} + H_2O \rightarrow OH_{ads} + H_2. \qquad (2b)$$

For both Co nitride and oxynitride, (2*a*) is heavily energetically favored relative to V oxynitride. This result would explain not only why Co oxides and oxynitrides are potent HER catalysts, but also explain the HER inactivity of V oxynitrides *at neutral pH*. It should be pointed out, however, that (to our knowledge) there are no data for HER of V oxynitrides under acidic conditions, where proton-based HER mechanisms might be expected to be relevant.

3. Summary and conclusions

The data presented herein provide the basis for several important conclusions regarding V oxynitride. The first is that an MVK mechanism is *not* operative under the conditions examined. Lattice N and solvated N_2, at pH 7, are both reduced to NH_3 by separate reaction mechanisms, both of which are favored at O-ligated vs. N-ligated V centers (Osonkie *et al* 2022). This has an important consequence in that, under any reasonable set of operating parameters at pH 7, the oxynitride should eventually be depleted of lattice N. At pH 7, V oxide is also NRR active (Ganesan *et al* 2021). Thus, in principle, one should not see a large fall-off over time of NRR activity for V oxynitrides as lattice N becomes depleted over time, and our electrochemistry studies support this conclusion. (Osonkie *et al* 2022). Existing data (Yang *et al* 2018, 2019) also suggest that V oxynitrides should exhibit NRR durability under acidic conditions.

At pH 7, V oxynitrides are also highly selective for NRR relative to HER. In fact (figure 16) they are HER inactive under neutral conditions (Chukwunenye *et al* 2022). However, the selectivity of NRR vs. HER for V oxynitrides *as a function of lattice N depletion*—as well as pH—remains to be explored. Indeed, experimental data (Dey *et al* 2019) suggest that V oxides (at least in +4/+5 oxidation states) are robust HER catalysts under acidic conditions. This finding is in accord with the results of DFT calculations discussed above, in that one would expect that the HER reaction pathway depending on O–H bond scission (equation (2*a*)) energetically unfavorable at V sites, should become less important at lower pH. Instead, a proton-based mechanism, e.g.:

$$H_3O^+ + e^- + {}^* \rightarrow {}^*H + H_2O \qquad (3a)$$

$${}^*H + H_2O\ (g) \rightarrow H_2\,(g)\ + {}^*OH. \qquad (3b)$$

is estimated to be energetically favored at V cation sites (Chukwunenye *et al* 2022). Thus, the above experimental and theoretical findings indicate that V oxynitride should be a robust NRR catalyst and highly selective for NRR over HER at pH 7, but that this selectivity should decrease at acidic conditions, at least for V in +4/+5 oxidation states (Dey *et al* 2019).

The above points to the importance of the V (or other transition metal) oxidation state in the process. Calculations of N≡N bond activation (figure 11) and NAP-XPS studies of N_2/V oxide interactions (figures 12–14) indicate that V(III) should be more active for N_2 activation than V(IV) or V(V). This could be due to the effects of V d electrons in π-backbonding (Balogun *et al* 2022), or the effects of different ligands associated with different oxidation states. Absent the depletion of lattice N, *ex situ* XPS data (e.g. figure 6) indicate that lattice N helps stabilize V in the +3 state, and that increasing V oxidation is observed after NRR and the loss of lattice N. Thus, stabilizing V in a lower (+3, vs. +4 or +5) might have real consequences for NRR activity and selectivity under acidic as well as neutral conditions.

The evident importance of metal oxidation states, as well as the lack of detailed experimental verification of reaction pathways, points toward the importance of surface science methods for future electrocatalysis-based studies. As shown above, in select cases, *ex situ* and *in situ* XPS, as well as NAP-XPS at the

vapor/solid interface can make important contributions to our understanding of transition metal oxidation state, as well as related aspects of catalyst surface composition, such as lattice N depletion. Indeed, preliminary *in situ* XPS results for other transition metal oxynitrides indicate that surface oxide formation/dissolution, as a function of pH, may also be key determinants in understanding pH effects on NRR activity. These data will be reported in a future publication. In the future, perhaps *operando* photoemission at the liquid–solid interface will also provide additional detailed information to bear on such issues.

Data availability statement

The data that support the findings of this study are available upon request from the authors.

Acknowledgments

The work at the UNT was supported by the National Science Foundation through Grant No. DMR-2112864. Additional NSF support for the UNT CASCaMHPC cluster via Grant No. CHE-1531468 is also gratefully acknowledged. NAP-XPS studies were carried out at the Advanced Light Source, which is a DOE Office of Science User Facility under Contract No. DE-AC02-05CH11231. PSB acknowledges support from U.S. Department of Energy, Office of Science, Office of Basic Energy Sciences, Chemical Sciences, Geosciences, and Biosciences (CSGB) Division through its Geosciences program at Pacific Northwest National Laboratory (PNNL). PNNL is a multi-program national laboratory operated for the DOE by the Battelle Memorial Institute under Contract No. DE-AC05-76RL01830.

ORCID iDs

Kabirat Balogun https://orcid.org/0000-0002-0416-928X
Slavomir Nemšák https://orcid.org/0000-0002-6103-2925
Paul S Bagus https://orcid.org/0000-0002-5791-1820
Jeffry A Kelber https://orcid.org/0000-0002-3259-9068

References

Ali-Löytty H *et al* 2016 *J. Phys. Chem.* C **120** 2247–53
Axnanda S *et al* 2015 *Sci. Rep.* **5** 9788
Balogun K *et al* 2022 *J. Chem. Phys.* **157** 104701
Becke A D 1997 *J. Chem. Phys.* **107** 8554–60
Biesinger M C, Lau L W M, Gerson A R and Smart R S C 2010 *Appl. Surf. Sci.* **257** 887–98
Briggs D and Seah M P 1990 *Practical Surface Analysis. Vol. 1—Auger and X-Ray Photoelectron Spectroscopy* (Chicester: Wiley)
Chukwunenye P, Ganesan A, Gharaee M, Balogun K, Anwar F, Adesope Q, Cundari T R, D'Souza F and Kelber J A 2022 *J. Mater. Chem.* A **10** 21401–15
Coulston G W, Thompson E A and Herron N 1996 *J. Catal.* **163** 122–9
Dey K K, Jha S, Kumar A, Gupta G, Srivastava A K and Ingole P P 2019 *Electrochim. Acta* **312** 89–99
Du H, Gengenbach T R, Hodgetts R, MacFarlane D R and Simonov A N 2019 *ACS Sustain. Chem. Eng.* **7** 6839–50
Eads C N *et al* 2020 *AIP Adv.* **10.** 085109
Emfietzoglou D and Nikjoo H 2007 *Radiat. Res.* **167** 110–20
Freund H, Kuhlenbeck H, Libuda J, Rupprechter G, Bäumer M and Hamann H 2001 *Top. Catal.* **15** 233
Frisch M J *et al* 2016 *Gaussian 16, Revision C.01* (Wallingford, CT: Gaussian, Inc)
Ganesan A, Osonkie A, Chukwunenye P, Rashed I, Cundari T, D'Souza F and Kelber J 2021 *J. Electrochem. Soc.* **168** 026504
Goodacre D *et al* 2020 *J. Chem. Phys.* **152** 044715
Hou J, Yang M and Zhang J 2020 *Nanoscale* **12** 69–692
Hubbard A T 1988 *Chem. Rev.* **88** 633–56
Humphreys J, Lan R and Tao S 2020 *Adv. Energy Sustain. Res.* **2** 200043
Jensen J A, Rider K B, Salmeron M and Somorjai G A 1998 *Phys. Rev. Lett.* **80** 1228–31
Kang S, Wang J, Zhang S, Zhao C, Wang G, Cai W and Zhang H 2019 *Electrochem. Commun.* **100** 90–95
Kelber J and Seshadri G 2001 *Surf. Interface Anal.* **31** 431–41
Kelly P J and Arnell R D 2000 *Vacuum* **56** 159
Kohn W and Sham L J 1965 *Phys. Rev.* **140** A1133–8
Kolasinski K W 2012 *Surface Science: Foundations of Catalysis and Nanoscience* (Chicester: Wiley)
Lee C, Yang W and Parr R G 1988 *Phys. Rev.* B **37** 785–9
Lee M *et al* 2020 *Adv. Mater. Technol.* **5** 2000592
Marenich A V, Cramer C J and Truhlar D G 2009 *J. Phys. Chem.* B **113** 6378–96
Moltved K A and Kepp K P 2019 *J. Phys. Chem.* C **123** 18432–44
Osonkie A, Ganesan A, Chukwunenye P, Anwar F, Balogun K, Gharaee M, Rashed I, Cundari T R, D'Souza F and Kelber J A 2022 *ACS Appl. Mater. Interfaces* **14** 531–42
Osonkie A, Lee V, Chukwunenye P, Cundari T and Kelber J 2020a *J. Chem. Phys.* **153** 144709
Osonkie A, Lee V, Oyelade A, Mrozek-mccourt M, Chukwunenye P, Golden T D, Cundari T R and Kelber J A 2020b *Phys. Chem. Chem. Phys.* **22** 24640–8
Padhan P, Sinha U K and Sahoo A 2018 *Rev. Sci. Instrum.* **89** 085102
Pan J, Hansen H A and Vegge T 2020 *J. Mater. Chem.* A **8** 2498–17
Qing G, Ghazfar R, Jackowski S T, Habibzadeh F, Ashtiani M M, Chen C, Smith M R III and Hamann T W 2020 *Chem. Rev.* **120** 5437–516
Salmeron M and Schlögl R 2008 *Surf. Sci. Rep.* **63** 169–99
Schnadt J, Knudsen J and Johansson N 2020 *J. Phys.: Condens. Matter* **32** 413003
Siegbahn K 1970 *Electron Spectroscopy for Chemical Analysis; Atomic Physics 3* vol 2 (Boston: Springer) pp 493–522
Sinfelt J H 2002 *Surf. Sci.* **500** 923
Somorjai G A and Li Y 2010 *Introduction to Surface Chemistry and Catalysis* (Hoboken, NJ: Wiley)
Soriaga M P 1992 *Prog. Surf. Sci.* **39** 325
Su X, Cremer P S, Shen Y R and Somorjai G A 1997 *J. Am. Chem. Soc.* **119** 3994–4000
Velasco-Vélez J *et al* 2021 *J. Appl. Phys.* **54** 124003
Vosko L H, Wilk A N L and Nusair D M 1980 *Can. J. Phys.* **58** 1200
Weigend F and Ahlrichs R 2005 *Phys. Chem. Chem. Phys.* **7** 3297–305
Yang X, Kattel S, Nash J, Chang X, Lee J H, Yan Y, Chen J G and Xu B 2019 *Angew. Chem., Int. Ed.* **58** 13768
Yang X, Nash J, Anibal J, Dunwell M, Kattel S, Stavitski E, Attenkofer K, Chen J G, Yan Y and Xu B 2018 *J. Am. Chem. Soc.* **140** 13387
Young S D, Ceballos B M, Banerjee A, Mukundan R, Pilania G and Goldsmith B R 2022 *J. Phys. Chem.* C **126** 12980